



A mechanistic explanation of the increase in particle scavenging in the ultrasonic scrubber



W. Ran, J.R. Saylor*

Clemson University, Department of Mechanical Engineering, Clemson, SC 29634, USA

ARTICLE INFO

Article history:

Received 19 December 2014

Received in revised form

8 May 2015

Accepted 13 May 2015

Available online 20 May 2015

Keywords:

Particle

Spray

Ultrasonics

Scrubbers

ABSTRACT

Ran et al., 2014 developed the ultrasonic scrubber, a device which combines an ultrasonic standing wave field and a water spray to eliminate particles from a gas flow. This device, which is essentially a wet scrubber enhanced by ultrasound, was shown to significantly improve the scavenging of micron-scale particles compared to the use of a water spray alone. Herein a simulation of trajectories of the particles and spray drops in the ultrasonic scrubber are presented. These simulations and an associated model of the process are used to provide a mechanistic understanding of the enhanced scavenging observed in the ultrasonic scrubber.

© 2015 Elsevier Ltd. All rights reserved.

1. Introduction

Emission from fossil fuel combustion in the transportation and industrial sectors is one of the main sources of particulate air pollution (Tucker, 2000). These particulate pollutants have significant deleterious effects on pulmonary health (Cohen, 2000; Docker & Pope, 1994; Pope et al., 1995; Pope et al., 2002; Schikowski et al., 2005; Schwartz et al., 1993; Seaton et al., 1995), cardiovascular disease (Johnson, 2004; Pope et al., 2004; Suwa et al., 2002; Verrier, Mittleman & Stone, 2002), and increased mortality (Schwartz & Dockery, 1992; Schwartz, Laden & Zanobetti, 2002). Particles with aerodynamic diameter less than 2.5 μm (PM_{2.5}) are believed to pose the greatest health risks (Davis, Bell & Fletcher, 2002; Schwartz et al., 1993).

Several methods exist for reducing particulate pollution from combustion sources. One example is the wet scrubber which has several advantages, including its ability to operate at high temperatures and to simultaneously remove gaseous and particulate pollutants. In a typical wet scrubber configuration, water is sprayed downward into an upward flowing stream of pollutant laden gas, and the pollutants are removed by the falling droplets which are collected at the bottom of the wet scrubber. The performance of a wet scrubber can be quantified by the scavenging coefficient:

$$E = \frac{n_s}{n_T} \quad (1)$$

where n_s is the number of particles removed by the scrubber, and n_T is the total number of particles entering the scrubber.

While generally effective, experimental and theoretical studies of wet scrubbers show that they perform poorly in the removal of micron-scale particles (Gemci & Ebert, 1992; Raj Mohan, Jain & Meikap, 2008). Plots of E versus particle diameter d_p for wet scrubbers typically show a minimum in the micron scale region. For example, Kim, Jung, Oh & Lee (2001) present

* Corresponding author. Tel.: +1 864 656 5621; fax: +1 864 656 4435

E-mail address: jsaylor@clemson.edu (J.R. Saylor).

URL: <http://myweb.clemson.edu/~jsaylor/index.html> (J.R. Saylor).

a plot of E versus d_p showing a minimum at (almost exactly) $d_p = 1 \mu\text{m}$. This minimum is due to the basic physics of particle collection which can be understood as follows. When a large particle approaches a droplet, its inertia prevents it from following the flow streamlines around the drop and the particle impacts the drop and is removed. For very small drops, this inertial effect vanishes, but Brownian motion causes these particles to deviate from their streamlines effectively diffusing to the drop. Inertial effects increase with d_p while Brownian motion decreases with d_p . Accordingly, there is a range of d_p falling between the inertially-dominant and diffusive-dominant regimes, where neither the inertial nor diffusive mechanisms are effective, resulting in a minimum in E , often referred to as the “Greenfield gap” (Greenfield, 1957). This minimum falls, again, within $0.1 \mu\text{m} \leq d_p \leq 10 \mu\text{m}$ as reported by several researchers (Gemci & Ebert, 1992; Kim et al., 2001; Lai, Dayan & Kerker, 1978; Lim, Lee & Park, 2006; Raj Mohan et al., 2008). Summarizing, the micron scale particle diameters that are most harmful to human lungs are the least effectively removed by wet scrubbers. Hence, there is a strong motivation to improve upon the current ability of wet scrubbers to remove micron scale particles from pollution streams.

Ran, Saylor, and Holt (Ran et al., 2014), referred to hereinafter as RSH, demonstrated that micron-scale particles could be more effectively removed when an ultrasonic standing wave field was added to the wet scrubber, a device which we term the “ultrasonic scrubber”. An ultrasonic standing wave field can be created by an ultrasonic transducer and a reflector (typically a flat metal disk), with the two separated by an integer number of half wavelengths. An example of such a setup is presented in Fig. 1 which shows a fine water mist being introduced into the standing wave field. The small drops are forced toward the pressure-nodal region by the acoustic radiation force, F_{ar} (see below), forming “accretion disks”. RSH hypothesized that particles in the vicinity of the standing wave field would also be driven to the accretion disks just as the fine water droplets are in Fig. 1 and that particles and drops would then come into close proximity with each other, increasing the chance for a drop to scavenge a particle, thereby increasing E . To test this hypothesis RSH used the small scale ultrasonic scrubber shown in Fig. 2, where air laden with fine particles was flowed into the scrubber. The particle concentrations of the inlet and outlet of the scrubber were measured to compute the scavenging coefficient E . Experiments conducted with and without the ultrasonic standing wave field showed an increase of as much as 140% due to the ultrasonics.

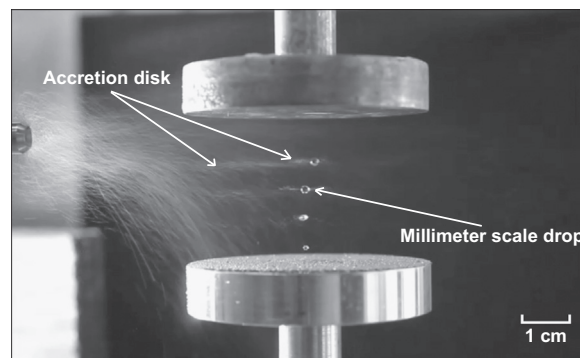


Fig. 1. Droplets accumulate in the accretion disks of an ultrasonic standing wave field. The ultrasonic horn is the lower circular aluminum piece and the reflector is the upper circular aluminum piece. A nebulizer can be seen on the left hand side, which introduces a fine water mist into the vicinity of the standing wave field. The large drops located in the center were formed by the agglomeration of these fine water mist drops.

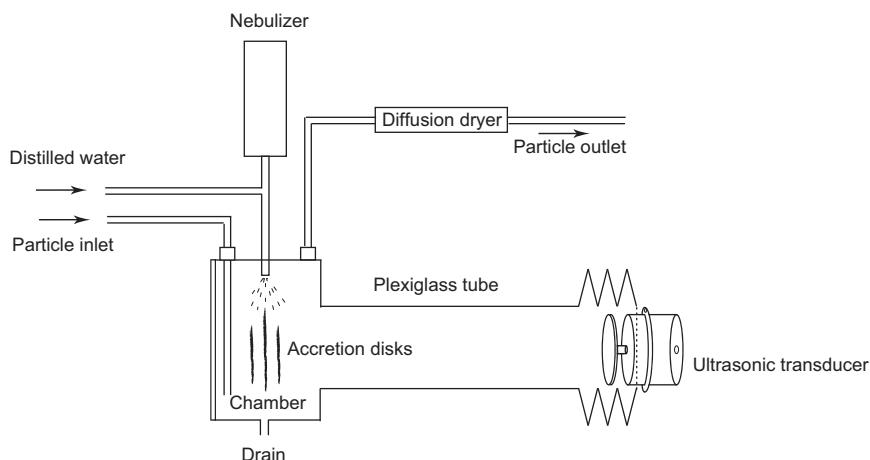


Fig. 2. Ultrasonic scrubber used by RSH. The scavenging chamber is the rectangular portion where the accretion disks are located and is presented in greater detail in Fig. 3. Note that the ultrasonic standing wave field is rotated 90° from that shown in Fig. 1. The diameter of the exit to the nebulizer at the top of the chamber is 2 mm.

These results suggest many exciting applications in the area of pollution control. However the mechanism for the ultrasonic improvement observed by RSH is unclear. RSH proposed three possible mechanisms that could potentially explain the increase in E . The first mechanism is based on the assumption that the acoustic radiation force significantly affects only the drops and that particles are entrained in the wakes of drops, bringing them into the accretion disks where the drop and particle number densities would increase, thereby increasing scavenging. The second and the third mechanisms are based on the assumption that the acoustic radiation force moves both drops and particles into the accretion zones. In the second mechanism, the increase in E is due to an increase in particles combining with each other in the accretion disks, while in the third mechanism, the increase is due to an increase in particles combining with drops.

Determining which, if any, of the above mechanisms is responsible for the improved performance of the ultrasonic scrubber is critical to the design and scale-up of this technology for actual applications, and is the goal of this paper. To achieve this goal, simulations of particle and drop trajectories in the ultrasonic scrubber are conducted and a model of the particle scavenging process is built.

2. Simulations

A schematic diagram of the ultrasonic scrubber used by RSH is shown in Fig. 2; it is mainly composed of a rectangular chamber, a plexiglass tube and an ultrasonic transducer. The chamber is the location where particle scavenging actually occurs; details of the size and geometry of the scavenging chamber are presented in Fig. 3. During the particle scavenging experiments conducted by RSH, air laden with polystyrene latex (PSL) microspheres was introduced from the bottom of the scavenging chamber while the spray was introduced from the top of the scavenging chamber. PSL spheres were used since they are readily available in a range of diameters and are fairly monodisperse. An ultrasonic standing wave field was created between the ultrasonic transducer at the far right side of the plexiglass tube and the reflector at the far left of the chamber. Under the influence of this standing wave field, the spray drops accumulated in the pressure-nodal region forming accretion disks as illustrated in Fig. 2. Note that the ultrasonic standing wave field and the accretion disks in the experimental setup are oriented 90° from those shown in Fig. 1. The interested reader is referred to RSH for more details on the ultrasonic scrubber.

In these simulations, three forces were considered to act on the particles and drops in the scavenging chamber: the acoustic radiation force F_{ar} (defined below), aerodynamic drag F_d , and the force due to gravity. Hence we ignore in this work any effects such as charging, phoretic effects, and particle–particle interactions. The simulations are of a single cross-section of the scavenging chamber which runs through the central axis of the standing wave field in the scavenging chamber and is illustrated as the shaded area in Fig. 4; the hatched area defines the area occupied by the standing wave field. This central

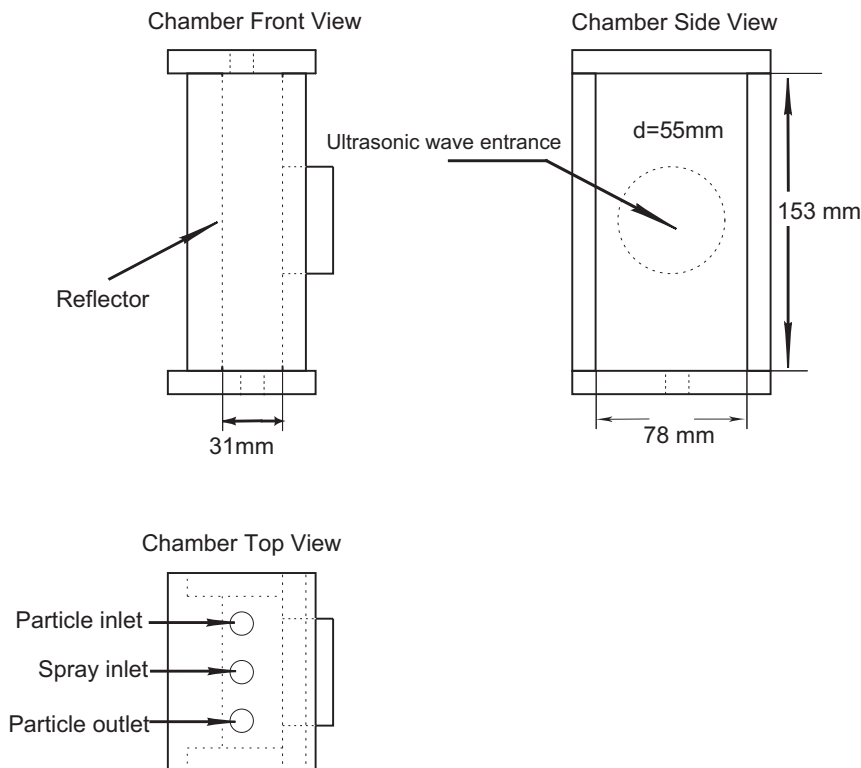


Fig. 3. Detailed view of the scavenging chamber.

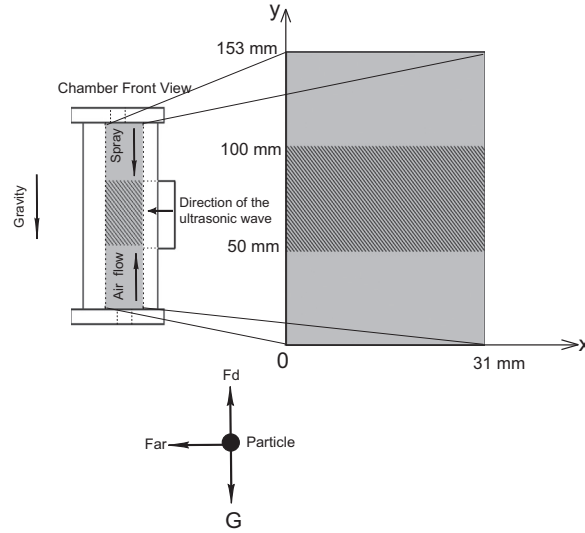


Fig. 4. Direction of the forces on a particle relative to the cross-section where the simulations are conducted. The shaded area represents the simulated domain. The hatched area represents the area occupied by the standing wave field.

cross section was chosen for simulation because, compared to other cross-sections, particles have the longest residence time in the standing wave field in this cross-section and therefore the improvement in scavenging due to ultrasonics is best exemplified by the dynamics occurring in this region. In this simulation domain, x is parallel to the direction of the acoustic wave. The spray drops enter the scavenging chamber from the top, traveling downward. It is assumed that these drops have only a y component of velocity as they enter the domain. Similarly, the particles and air flow enter the chamber from the bottom and travel upward and in the simulations they are assumed to have only a y velocity component as well. Of course the particles, drops, and air flow in RSH likely had a non-zero component of velocity in the x direction, but this would have been small. F_{ar} is assumed to act solely in the x direction and is the only force causing the trajectories of the particles and drops to deviate from a perfectly vertical path. We note that F_{ar} is the primary acoustic radiation force and that there is also a lateral acoustic radiation force that would act in the y direction. However the lateral acoustic radiation force is estimated to be orders of magnitude smaller than the primary radiation force (Hancock, 2001) and is not considered here.

The acoustic radiation force is estimated based on the theory of Settneß & Bruus (2012) who predict F_{ar} for a standing wave field:

$$F_{ar} = F_{max} \sin(2kx), \quad (2)$$

where

$$F_{max} = \frac{1}{2} \pi \Phi \left(\frac{\kappa_p}{\kappa}, \frac{\rho_p}{\rho}, \frac{2\delta}{d} \right) k E_{ac} d^3, \quad (3)$$

$$\Phi \left(\frac{\kappa_p}{\kappa}, \frac{\rho_p}{\rho}, \frac{2\delta}{d} \right) = \frac{1}{3} f_1 \left(\frac{\kappa_p}{\kappa} \right) + \frac{1}{2} f_2 \left(\frac{\rho_p}{\rho}, \frac{2\delta}{d} \right), \quad (4)$$

$$f_1 \left(\frac{\kappa_p}{\kappa} \right) = 1 - \frac{\kappa_p}{\kappa}, \quad (5)$$

$$f_2 \left(\frac{\rho_p}{\rho}, \frac{2\delta}{d} \right) = \Re \left[\frac{2 \left[1 - \gamma \left(\frac{2\delta}{d} \right) \right] \left(\frac{\rho_p}{\rho} - 1 \right)}{2 \frac{\rho_p}{\rho} + 1 - 3\gamma \left(\frac{2\delta}{d} \right)} \right], \quad (6)$$

$$\gamma \left(\frac{2\delta}{d} \right) = -\frac{3}{2} \left[1 + i \left(1 + \frac{2\delta}{d} \right) \right] \frac{2\delta}{d}, \quad (7)$$

$$\delta = \sqrt{\frac{2\nu}{\omega}}, \quad (8)$$

where E_{ac} is the acoustic energy density, d is the diameter of the particle or drop, $k = 2\pi/\lambda$, where λ is the wavelength, ρ is the air density, ρ_p is the density of the particle, κ is the compressibility of the air, κ_p is the compressibility of the particle, ν is the kinematic viscosity of the air, and ω is the angular frequency of the ultrasonic standing wave field. Details regarding the

specific values used in Eqs. (2)–(8), and how they were obtained, can be found in RSH. We note that E_{ac} was obtained empirically in RSH and that value is used here. So in using Eqs. (2)–(7) we have “calibrated” our simulations to agree in magnitude with those of RSH and avoided the problem of relating the power delivered to the transducer to the acoustic power in the standing wave field.

The aerodynamic drag force F_d is calculated assuming Stokes flow around the particle or drop:

$$F_d = 3\pi\nu\rho Ud \quad (9)$$

where U is the relative velocity between the particle and the air flow. To justify the Stokes' flow assumption, the maximum x and y direction velocities were estimated by equating the drag to F_{ar} in the x direction and equating the drag force to gravity in the y direction. Assuming a particle diameter of $\sim 1 \mu\text{m}$, and a drop diameter of $\sim 100 \mu\text{m}$, and assuming the $F_{ar} = F_{max}$, gives a maximum velocity of 10^{-2} m/s for the particle and 10^{-1} m/s for the drop which correspond to Reynolds numbers Re of 10^{-3} and 1, respectively, justifying the Stokes flow assumption for both particles and drops. We note that for the particles, some degree of slip is present. The largest Knudsen number is for the $0.7 \mu\text{m}$ PSL particles and was 0.14. The Cunningham slip correction factors ranged from 1.06 for the $4.2 \mu\text{m}$ particles to 1.36 for the $0.7 \mu\text{m}$ particles (Davies, 1945; Hinds, 1982). Hence, in the worst case scenario, Eq. (9) overpredicts the drag force on the particles by 36% which was assumed acceptable in light of the other assumptions made here. There is also the possibility that viscous effects of one particle or drop on another will impact the simulated trajectories. This is almost certainly the case in the accretion disks where the concentrations of particles and drops are expected to be high. However, for this preliminary model development, such effects are ignored and left as future work. It is noted that at the highest inlet concentrations explored in these simulations, the average distance between any drop or particle is about $460 \mu\text{m}$. Considering a $100 \mu\text{m}$ drop undergoing Stokes flow, the ratio of the Stokes drag in an infinite medium to that influenced by another particle $460 \mu\text{m}$ away is about 85% (Happel & Brenner, 1965; Panton, 1984). While this is not a large effect in light of other assumptions made, again, in the accretion disks, this effect is likely to be higher and should be explored in future work.

The small Reynolds numbers cited above can also be used to narrow down the possible mechanisms for explaining the results of RSH. As noted in the Introduction above, the first mechanism postulated by RSH to explain the increase in scavenging due to ultrasonics is that particles are entrained in the wakes of drops as they are moved to the accretion zones by the acoustic radiation force. This mechanism can now be excluded (even prior to the simulations to be presented below) because experimental results (Taneda, 1956) and simulations (Zamyshlyaev & Shrager, 2004) from the literature show that the wake behind a drop does not appear until $Re > 20$ and Re for the drops are of $\mathcal{O}(1)$. With one possible mechanism excluded, the remaining two mechanisms are the following: particles combining with each other in the accretion disks or particles combining with drops in the accretion disks.

Balancing the gravitational, drag, and acoustic forces gives the following equations which can be numerically solved to provide the particle and drop trajectories:

$$m\ddot{x} = \begin{cases} F_{ar} - 3\pi\nu\rho d\dot{x} & (50 \text{ mm} < y < 100 \text{ mm}) \\ -3\pi\nu\rho d\dot{x} & (\text{otherwise}) \end{cases} \quad (10)$$

and

$$m\ddot{y} = -mg + 3\pi\nu\rho d(U_g - \dot{y}) \quad (11)$$

where m is the particle/drop mass, d is the particle/drop diameter, U_g is air velocity, (x,y) is the particle/drop location, and dotted quantities imply derivatives with respect to time. Equation (10) is a two-part equation since F_{ar} only acts in the central part of the domain as shown in Fig. 4.

We note that several assumptions are made in the above approach. First, F_{ar} is assumed to be perfectly one dimensional. Secondly, the particle, drop, and air velocities entering the simulation domain are assumed to be one dimensional as well, having only a y -direction component. Finally, many forces and processes other than those considered here could potentially affect the performance of the ultrasonic scrubber. These include particle deposition on the walls, viscous effects of one particle or drop on the other, air motion induced by particle/drop motion, charge effects, and polydispersity of the drops and particles. These factors are ignored here so that the interaction only of the acoustic force, gravity, and drag may be carefully explored.

Equations (10) and (11) were solved numerically using the explicit Runge–Kutta method (Hoffmann & Chiang, 2000) using the Matlab programming language with a maximum relative error of 0.1% (the estimated error of the numerical method at each time step divided by the solution at that time step). The simulated particle and drop trajectories are presented below.

3. Results

A sample simulation is shown in Fig. 5 where 50 PSL particles and 50 spray drops are initially introduced from the bottom ($y=0$ mm) and the top ($y=153$ mm) of the domain, respectively, spaced $\lambda/20$ apart in the x -direction. The PSL particles entered the domain at the same velocity as the air U_g , directed upward. The drops entered with a vertical velocity of 0.13 m/s, directed downward. This velocity was obtained by dividing the water spray flow rate by the cross-sectional area of the nebulizer nozzle. The initial horizontal velocity was set to zero for both PSL particles and spray drops. The other

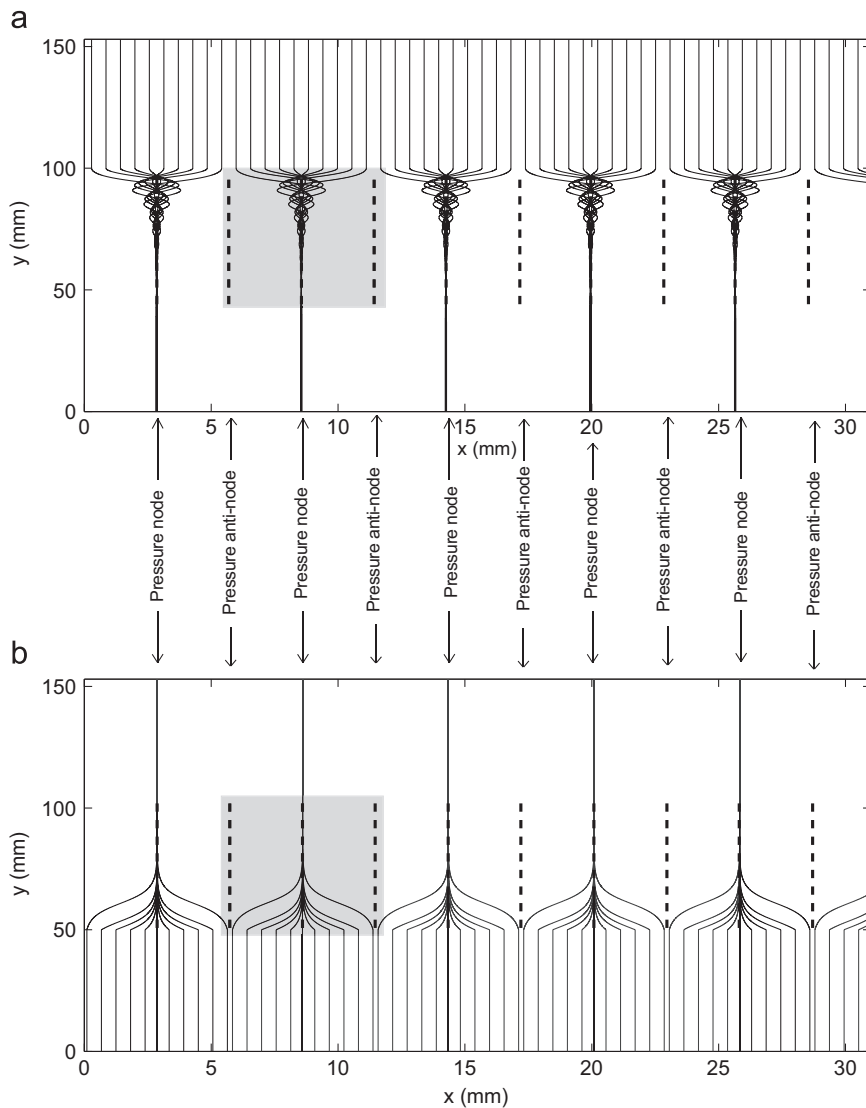


Fig. 5. The simulated trajectories of the drops (a) and the PSL particles (b). Solid lines are trajectories, dashed lines are pressure nodes (accretion disks) or pressure anti-node locations. A detailed view of these trajectories around a single pressure node (shaded areas) is presented in Fig. 9. Note that the domains of (a) and (b) are identical.

parameters are the same as for typical conditions in the experiments of RSH: $d_p = 0.9 \mu\text{m}$, $d_d = 87 \mu\text{m}$, and $U_g = 2.8 \text{ cm/s}$. Figure 5 shows an interesting difference between the motion of the particles and drops in the standing wave field. The particles immediately approach the pressure nodes (accretion disks) without overshooting, while the drops overshoot multiple times; an over-damped and under-damped oscillation, respectively.

The trajectories of drops having a range of diameters comparable to those explored in the experiments of RSH are presented in Fig. 6 (unlike Fig. 5 only a single pressure node (accretion disk) is presented). The trajectories presented in Fig. 6 show that the length of the trajectory over which overshooting of the node occurs increases with drop diameter, and actually includes the entire simulation domain for the largest drop diameter ($d_d = 97 \mu\text{m}$) considered. Overshooting occurs for all diameters explored in this figure, though it is difficult to see in Fig. 6(a) (but can be seen in the expanded inset). The trajectories for PSL particles having a range of diameters comparable to those explored in RSH are presented in Fig. 7, showing overdamped trajectories in all cases.

The trajectories of PSL particles and spray drops for the range of air velocities U_g explored in RSH are presented in Fig. 8. The air velocities are estimated by dividing the air flow rates used in the experiments by the cross-sectional area of the scavenging chamber. Figure 8 shows that the trajectories of the drops are not significantly affected by U_g while the particle trajectories are affected by the air velocity. The figure shows that the larger U_g is, the farther the particle trajectories extend into the domain before F_{ar} forces them into the accretion zone.

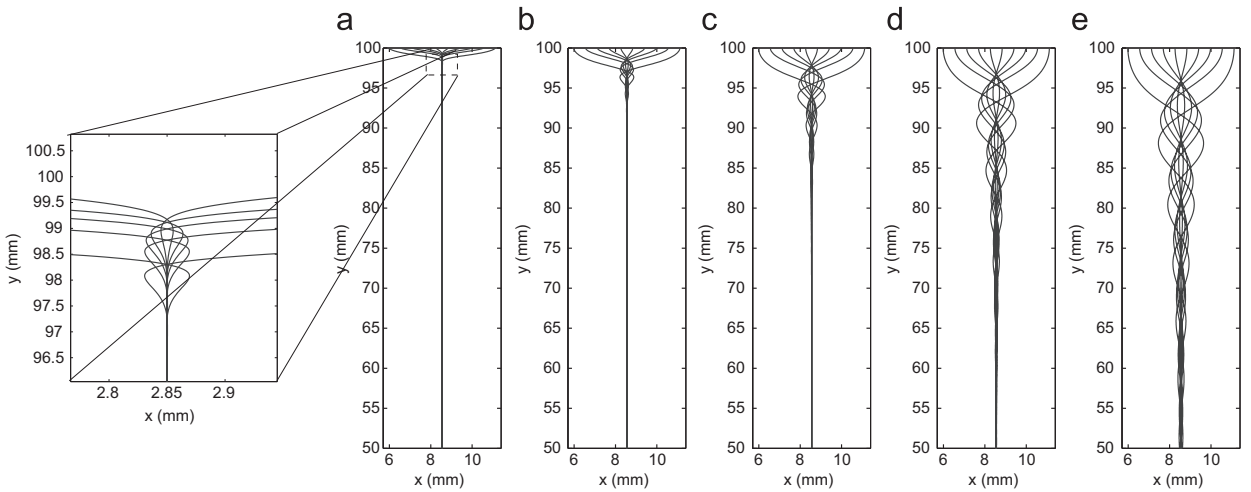


Fig. 6. The simulated trajectories of the drops with different diameters for a single pressure node. (a) $d_d = 40 \mu\text{m}$. (b) $d_d = 56 \mu\text{m}$. (c) $d_d = 71 \mu\text{m}$. (d) $d_d = 87 \mu\text{m}$. (e) $d_d = 97 \mu\text{m}$. $U_g = 2.8 \text{ cm/s}$ for all cases in this figure.

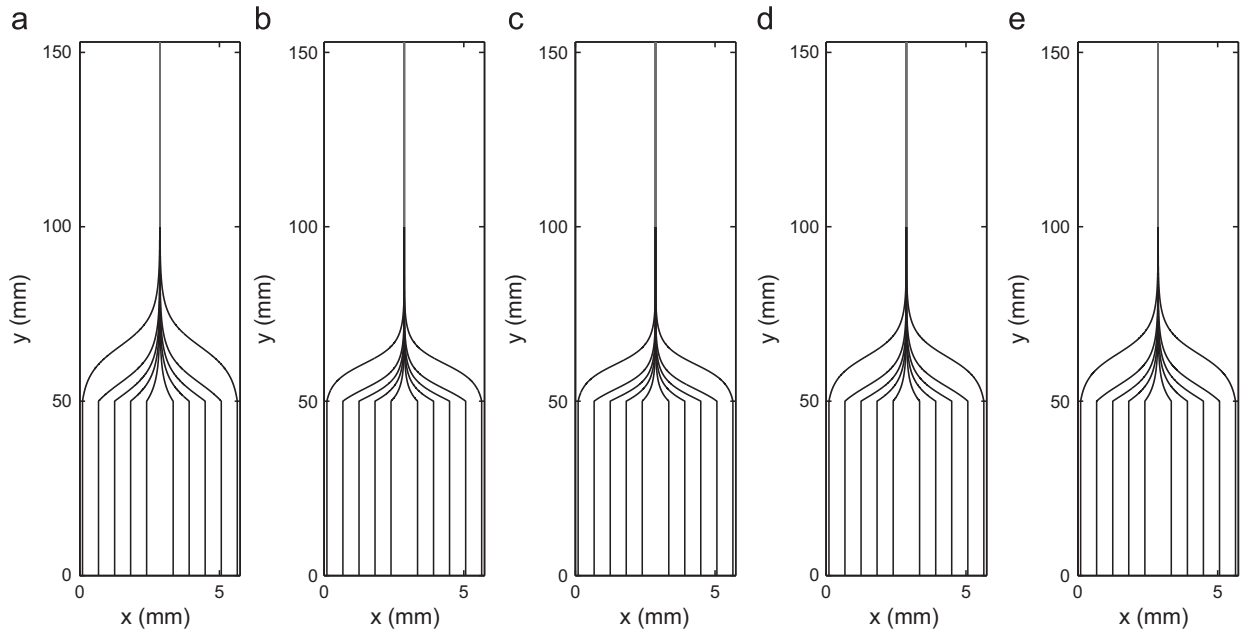


Fig. 7. The simulated trajectories of the particles with different diameters. These diameters were used in the scavenging experiments of RSH: (a) $d_p = 0.7 \mu\text{m}$. (b) $d_p = 0.9 \mu\text{m}$. (c) $d_p = 2.3 \mu\text{m}$. (d) $d_p = 3.1 \mu\text{m}$. (e) $d_p = 4.2 \mu\text{m}$. $U_g = 2.8 \text{ cm/s}$ for all cases in this figure.

4. Discussion

Referring to Figs. 5–8, it is clear that for all the conditions explored by RSH, F_{ar} causes significant motion of both the PSL particles and the drops since both are driven into the accretion disk by F_{ar} . However, it remains unclear whether the increased scavenging observed by RSH is due to an increase in particles combining with each other, and/or particles combining with drops. The following analysis is developed to reveal which of these mechanisms is dominant.

Figure 5 shows that as drops/particles travel through the standing wave field, their trajectories become closer together, increasing their number concentrations. We quantify this concentration via the width of the envelope that bounds all of the trajectories, W , which is a function of y . This envelope is plotted in Fig. 9 along with the trajectories within the envelope for both the particles and drops. The domain considered is the region bounded by two pressure anti-nodes with a pressure node at the region's center (the shaded areas in Fig. 5). The increase in the concentration of the drops or particles as they travel through the field can be quantified as W_0/W where W_0 is the value of W at the entrance to the standing wave field.

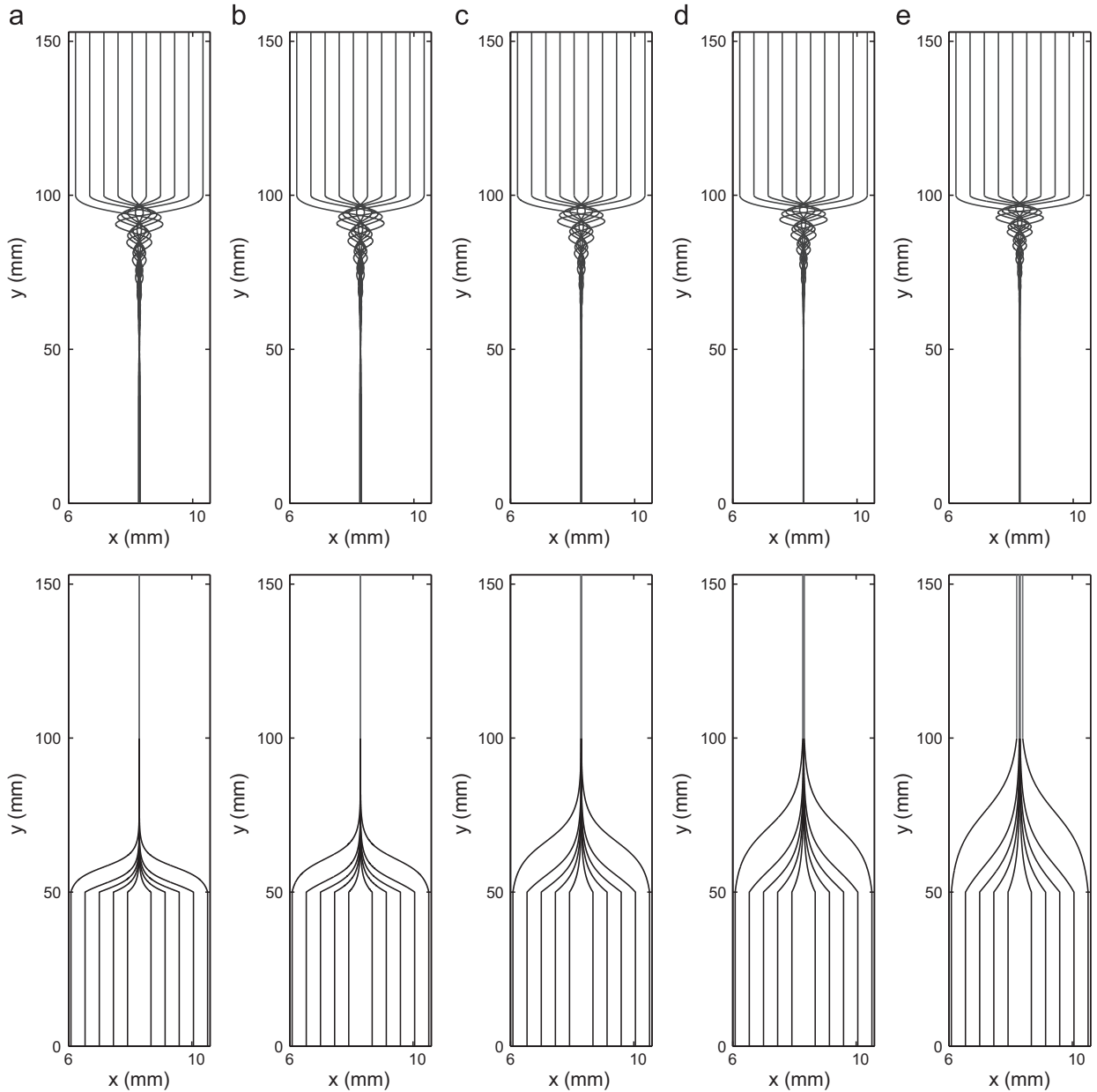


Fig. 8. The simulated trajectories of the drops (top) and the PSL particles (bottom) around a single pressure node under varying air flow velocity U_g . (a) $U_g = 2.1$ cm/s. (b) $U_g = 2.8$ cm/s. (c) $U_g = 4.2$ cm/s. (d) $U_g = 5.4$ cm/s. (e) $U_g = 6.7$ cm/s. These air velocities were used in the scavenging experiments of RSH. In these simulations, $d_p = 0.9 \mu\text{m}$ and $d_d = 87 \mu\text{m}$.

Therefore, the concentration of particles at any y location can be quantified as

$$C = C_0 \frac{W_0}{W} \quad (12)$$

where C_0 is the concentration of the particles at W_0 for the actual experiments. The simulations of the conditions explored by RSH show that the maximum value of W_0/W is $\mathcal{O}(10^4)$, at $d_p = 0.9 \mu\text{m}$, $U_g = 2.1$ cm/s. Given that the highest C_0 for particles in the experiments of RSH was $4 \times 10^7/\text{m}^3$, a maximum particle concentration in those experiments is $C \sim 4 \times 10^{11}/\text{m}^3$.

To determine whether, and to what extent, the increased scavenging observed in RSH was due to particle–particle interaction, we now consider the collision and combination of particles with each other caused by Brownian motion, for the maximum concentration computed above. The decrease of particle number concentration with time for monodisperse

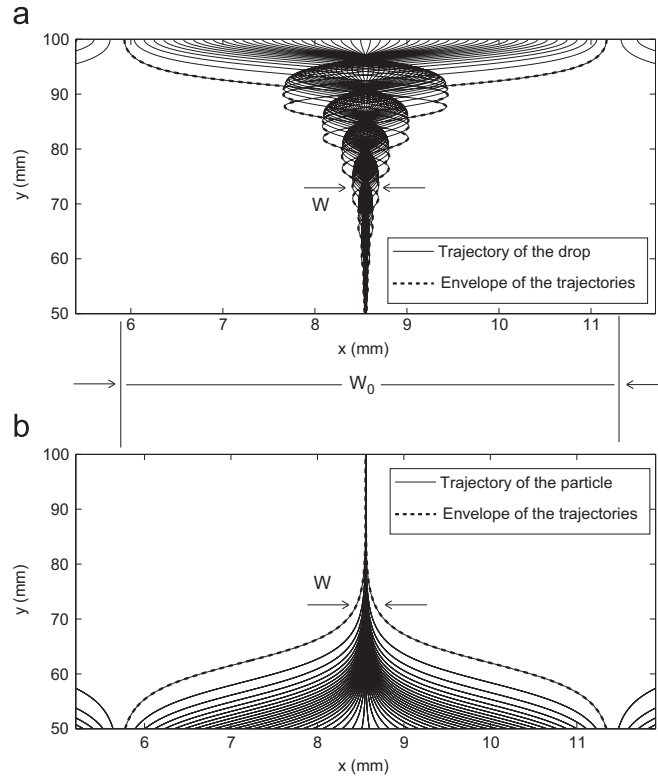


Fig. 9. (a) Envelope of the trajectories of the drops ($d_p = 87 \mu\text{m}$). (b) Envelope of the trajectories of the particles ($d_p = 0.9 \mu\text{m}$). $U_g = 2.8 \text{ cm/s}$ for both (a) and (b).

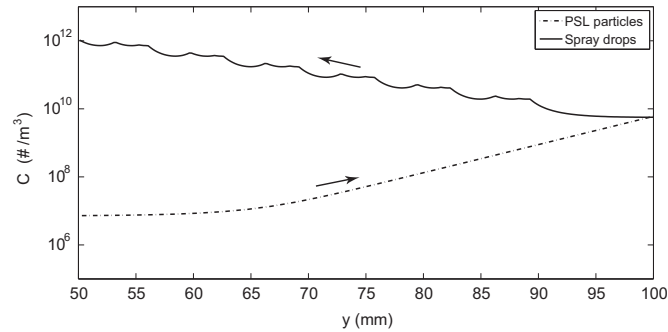


Fig. 10. The number concentration versus y for particles and drops in the pressure node. Here $d_p = 0.9 \mu\text{m}$, $d_d = 87 \mu\text{m}$, $U_g = 2.8 \text{ cm/s}$ and $Q_l = 0.92 \text{ ml/s}$. The arrows indicate the direction of travel of the particles/drops.

particles due to interparticle combination by Brownian motion is well studied and can be described as (Hinds, 1999)

$$E_B = \left(1 - \frac{1}{1 + C_{t_0} K(t - t_0)}\right) \times 100\% \quad (13)$$

where E_B is the percent decrease of particle number concentration, C_{t_0} is the particle concentration at time t_0 , t is time, and K is the particle coagulation coefficient, which for $0.9 \mu\text{m}$ particles at standard conditions is $3.4 \times 10^{-16} \text{ m}^3/\text{s}$ (Hinds, 1999). The above equation is derived using the assumptions that every particle collision leads to a combination, that for each combination there is a reduction of one in the number of particles, and that particle combinations do not change the particle size distribution. For monodisperse particles with $d_p = 0.9 \mu\text{m}$ and $C_{t_0} = 4 \times 10^{11} / \text{m}^3$, Eq. (13) predicts a decrease in particle concentration of only 0.1% in 10 s. The longest particle residence time in these simulations was 7.5 s. The assumptions used in deriving Eq. (13) are conservative in the sense that they maximize the loss of particles; accordingly, particle–particle interactions are not likely to cause the increased scavenging observed in the experiments of RSH.

Of the mechanisms described in the introductory section for explaining the increase in scavenging due to ultrasonics, the only one left is an increase in particles combining with drops. Since, it is possible that some other, unknown mechanism could be the cause, we seek to go beyond a process-of-elimination proof that particles combining with drops are the cause

of increased scavenging. Specifically, we now build a model of the increased scavenging based on the presumption of a particle–drop mechanism, and then compare the model’s predictions with the results presented in RSH. Though the model does not predict explicitly a scavenging coefficient, it is used to evaluate how the scavenging coefficient varies with experimental conditions; then these are compared with the way the increased scavenging observed by RSH varies with experimental conditions.

To begin this model, the number concentration of particles and drops is needed. This is obtained from Eq. (12) where C_0 for the drops is obtained using the water flow rate from RSH Q_l and assuming that the drops all have the average drop diameter d_d . Values of C_0 for the particles were obtained from the measurements of RSH. An example plot of C versus y for particles and drops is presented in Fig. 10, for the case where $d_p = 0.9 \mu\text{m}$, $d_d = 87 \mu\text{m}$, $U_g = 2.8 \text{ cm/s}$ and $Q_l = 0.92 \text{ ml/s}$ which shows that the particle concentration increases with y while the spray drop concentration decreases with y . This is simply because the particles enter the standing wave field from the bottom of the scavenging chamber while the drops enter from the top, as shown in Fig. 5. The intersection of the particle and spray concentrations at $y = 100 \text{ mm}$ is coincidental.

The potential particle/drop collision frequency per unit volume is (Hinds, 1999)

$$f_c = K_c C_p C_d, \tag{14}$$

where C_p and C_d are the particle and drop number concentration at any given y , respectively, and K_c is the collision coefficient, which quantifies the rate of collisions between particles and drops in a certain volume of space, and has units of m^3/s . To apply Eq. (14) in the accretion disks, account must be taken of the fact that the envelopes containing the particles and drops do not occupy the same volume. This is illustrated in Fig. 11 which shows the overlapped trajectories of particles and drops revealing that in some y locations, W is smaller for the drops than for the particles. In these locations, only a portion of the particles are exposed to drops. To account for this, Eq. (14) is rewritten as

$$f_c = \begin{cases} K_c C_p C_d \frac{W_d}{W_p} & (W_d < W_p) \\ K_c C_p C_d & (\text{otherwise}) \end{cases} \tag{15}$$

In Eq. (15), when $W_d < W_p$, the width of the trajectories of the drops is smaller than the width of the trajectories of the particles and so only a portion of the particles are exposed to drops; so f_c must be reduced accordingly.

The variable f_c is the *potential* collision frequency. Particles and drops on a collision course will not necessarily combine due to issues described in the Introduction, namely the lack of inertia in a particle may cause it to follow the streamline it is on and not combine with the particle. Other issues also can cause a drop and particle on a collision course to not actually combine. Whether or not a particle on a collision path with a drop will combine with the drop is quantified by the scavenging coefficient for a single drop:

$$E_s = \frac{n_1}{n_2} \tag{16}$$

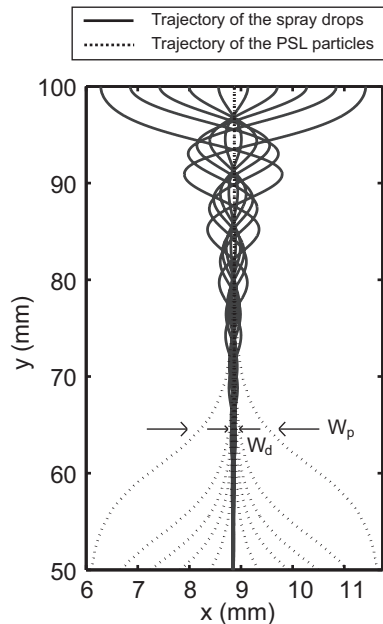


Fig. 11. Overlapped trajectories of particles and drops. Here $d_p = 0.9 \mu\text{m}$, $d_d = 87 \mu\text{m}$, and $U_g = 2.8 \text{ cm/s}$.

Where n_2 is the total number of particles on a collision path with the drop and n_1 is the number of particles that will eventually combine with the drop. E_s is a complex function of the size of the particle and the drop, their relative velocity, and other parameters (Slinn, 1984). Knowing E_s , one can estimate the rate of particle scavenging by drops per unit volume at a location y in the accretion disks as

$$S = f_c E_s \quad (17)$$

The rate of particle scavenging by drops per unit volume for the accretion disks, \bar{S} , is estimated by taking the average of S over the whole accretion disk:

$$\bar{S} = \frac{\int_{y_1}^{y_2} S dy}{y_2 - y_1} = \frac{\sum_{y=y_1}^{y_2} S \Delta y}{y_2 - y_1} \quad (18)$$

where y_1 and y_2 are the locations at either end of the accretion disk. The second portion of Eq. (18) was used here due to the discrete nature of the simulations. For the case shown in Fig. 10, $y_1 = 50$ mm and $y_2 = 100$ mm and $\Delta y = 0.05$ mm. By combining Eqs. (15), (17) and (18) and assuming that E_s and K_c are not a function of y yield

$$\bar{S} = \begin{cases} E_s K_c \frac{\sum_{y=y_1}^{y_2} C_p C_d \frac{W_d}{W_p} \Delta y}{y_2 - y_1} & (W_p > W_d) \\ E_s K_c \frac{\sum_{y=y_1}^{y_2} C_p C_d \Delta y}{y_2 - y_1} & (\text{otherwise}) \end{cases} \quad (19)$$

Since the ultrasonic scrubber is operated in a nominally steady-state condition, the variables on the right hand side of Eq. (19) are constant in time. Hence, \bar{S} also does not vary with time, and E_p , the scavenging coefficient of particles by drops in the accretion disk, can be expressed as

$$E_p = \frac{\bar{S} t_s}{C_{p0}} = \begin{cases} E_s K_c t_s \frac{\sum_{y=y_1}^{y_2} C_p C_d \frac{W_d}{W_p} \Delta y}{(y_2 - y_1) C_{p0}} & (W_d < W_p) \\ E_s K_c t_s \frac{\sum_{y=y_1}^{y_2} C_p C_d \Delta y}{(y_2 - y_1) C_{p0}} & (\text{otherwise}) \end{cases} \quad (20)$$

where t_s is the time the particles reside in the ultrasonic standing wave field, and C_{p0} is the concentration of the particles before they enter the ultrasonic standing wave field. While many studies exist giving values for K_c and E_s , none are for the same conditions as RSH, and there is also significant scatter in these reported values. Without E_s and K_c , E_p cannot be obtained explicitly. However, we can write

$$E_p = \Lambda E_s K_c \quad (21)$$

where

$$\Lambda = \begin{cases} \frac{t_s \sum_{y=y_1}^{y_2} C_p C_d \frac{W_d}{W_p} \Delta y}{C_0 (y_2 - y_1)} & (W_d < W_p) \\ \frac{t_s \sum_{y=y_1}^{y_2} C_p C_d \Delta y}{C_0 (y_2 - y_1)} & (\text{otherwise}) \end{cases} \quad (22)$$

which gives

$$E_p \propto \Lambda \quad (23)$$

if Λ does not vary with E_s and K_c . So, while exact values for E_p cannot be computed and compared to those obtained in RSH, we can compare the way that E_p varies with experimental conditions for both the simulations and the RSH experiments. However, all of this hinges on the assumption that E_s and K_c remain unchanged. Unfortunately, E_s and K_c do change when particle diameter d_p or drop diameter d_d is varied, which complicates comparison of the present model with the results of RSH. However, as we now show, E_s and K_c do not change as the air flow rate Q_g and water flow rate Q_l are varied, enabling a relatively robust comparison of the model developed here and the results of RSH for variations in these two parameters.

Based on the scavenging theory of Slinn (1984), E_s is a function of several parameters, but varies most with Stokes number:

$$Stk = \frac{\rho_p U_{pd} d_p^2}{9\nu d_d} \quad (24)$$

where ρ_p is the density of the particle, U_{pd} is the relative velocity between the particle and the drop, and ν is the kinematic viscosity of the surrounding gas. Therefore, Stk will not be affected when the water flow rate, Q_l , is varied. It is possible that when the air flow rate, Q_g , is varied, Stk may vary since U_{pd} may change with Q_g . However, the simulations show that the

drops used in the experiments are falling at their terminal velocity in the y -direction when they enter the ultrasonic standing wave field (shaded region in Fig. 5). That is, the absolute velocity of the drop in the y -direction is

$$U_d = U_g - \frac{m_d g}{3\pi\nu\rho d_d} \quad (25)$$

where U_g is the air velocity in the y -direction and m_d is the mass of the drop. The same is true of the particle:

$$U_p = U_g - \frac{m_p g}{3\pi\nu\rho d_p} \quad (26)$$

where m_p is the mass of the particle. Therefore, the relative velocity between the particle and the drop, U_{pd} , is

$$U_{pd} = U_d - U_p = -\frac{m_d g}{3\pi\nu\rho d_d} + \frac{m_p g}{3\pi\nu\rho d_p} \quad (27)$$

The above equation shows that U_{pd} is independent of Q_g , so Stk , and therefore E_s , is independent of Q_g .

The parameter K_c varies according to the existence and magnitude of the mechanisms which can cause a drop–particle velocity differential, e.g. difference in diffusion rate, difference in inertia, difference in electrostatic mobility, and turbulence (Allen & Smith, 2001; Hinds, 1999; Lee & Chen, 1984; Otto & Fissan, 1999). Because the potential electrostatic charges on the particles were neutralized and Re of the flow in the scavenging chamber (assuming the chamber is a rectangular pipe) was ~ 60 in the experiments of RSH, the effect of difference in electrostatic mobility and the effect of turbulence can be excluded. Therefore, in the experiments of RSH, it can be assumed that the mechanisms that cause the relative motion between the particle and the drop are due to the difference in their diffusion rate and inertia. The diffusion rate and inertia of the particle and the drop are dependent on their diameters, (d_p, d_d). Accordingly, we can conclude that, like E_s, K_c remains unchanged for varying air flow rate Q_g or water flow rate Q_l , but does change when particle diameter d_p or drop diameter d_d is varied.

Given the above, a comparison can be made of how Λ (which is proportional to E_p) varies with Q_g and Q_l for the results of RSH and the present model. For each experiment presented by RSH a scavenging coefficient was measured with and without the ultrasonic standing wave field, E_w and E_{wo} , allowing quantification of the increase in scavenging due to ultrasonics as

$$E_I = E_w - E_{wo}, \quad (28)$$

which we compare to Λ here. Figure 12 is a plot of E_I versus Λ for a range of air flow rates Q_g and water flow rates Q_l . The particle size d_p and drop size d_d are fixed at $0.9 \mu\text{m}$ and $87 \mu\text{m}$, respectively. This plot shows that Λ obtained from the model presented above and E_I obtained from RSH are positively correlated to each other. Therefore, since Λ is linearly related to E_p (at least under the assumptions cited above), E_I must also be positively correlated to E_p . Because E_p is the scavenging coefficient of particles by drops in the accretion disks, and E_I quantifies the increased particle scavenging due to the standing wave field observed by RSH, this provides additional evidence that the increased scavenging is due to an increase in particles combining with spray drops in the accretion disks. This supports this mechanism beyond the process of elimination argument presented earlier.

The last part of this paper is an attempt to predict E_I for the ultrasonic scrubber outside the parameter space investigated by RSH using the correlation between E_I and Λ established above. The parameter considered here is the particle concentration, because the particle concentrations of uncontrolled industrial emissions are much higher than those used in RSH where the largest particle concentration upstream of the ultrasonic scrubber was $4 \times 10^7/\text{m}^3$, while the concentrations of fine particles ($d_p \sim 1 \mu\text{m}$) of uncontrolled industrial emissions range from $10^{10}/\text{m}^3$ to $10^{13}/\text{m}^3$ (Shannon et al., 2013). Considering these larger particle concentrations, and keeping other parameters the same

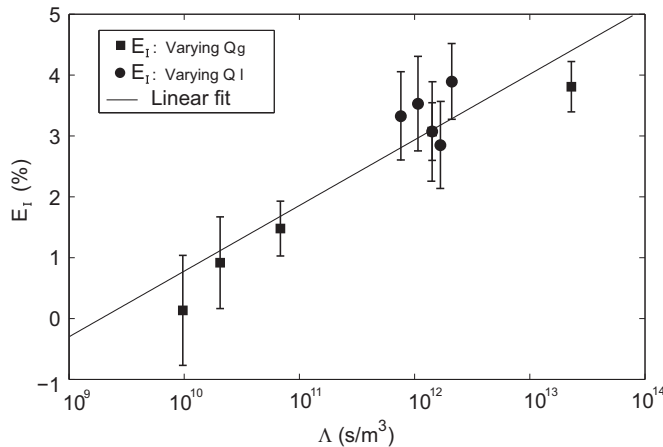


Fig. 12. Plot of E_I versus Λ for varying air flow rate Q_g and varying water flow rate Q_l . The particle size d_p and drop size d_d are fixed at $0.9 \mu\text{m}$ and $87 \mu\text{m}$ respectively.

($d_p=0.9\ \mu\text{m}$, $d_d=87\ \mu\text{m}$, $Q_l=0.92\ \text{ml/s}$ and $Q_g=67\ \text{ml/s}$), then Λ calculated using Eq. (22) increases to 10^{22} – $10^{25}\ \text{s/m}^3$ from $\sim 10^{10}$ – $10^{14}\ \text{s/m}^3$. This is a significant increase. The data presented in Fig. 12 give the following relation between E_l and Λ :

$$E_l = 1.18\log_{10}\Lambda - 11.27, \quad (29)$$

which predicts that E_l for particle concentrations typically found in industrial emissions increases to 15–18%. Moreover, we have reason to believe that E_l could be even higher than this estimate. This is because the effect of particle–particle interactions is not considered in the estimation of E_l in Eq. (29). Though particle–particle interactions were shown to be negligible for the particle concentrations investigated by RSH, at the higher particle concentrations found in industrial emissions, particle–particle interactions are significant. If the ultrasonic scrubber is used to treat industrial emissions, and assuming that other parameters are the same as the typical experiments of RSH, consideration of particle–particle interactions alone gives E_B ranging from 3% to 97% (using Eqs. (12) and (13)), which is comparable or larger than E_l estimated based only on the particle–drop interactions. Hence, further research on the use of the ultrasonic scrubber at significantly higher particle concentrations than those explored by RSH is needed.

5. Conclusion

The work presented in this paper demonstrated that the enhanced scavenging caused by an ultrasonic standing wave field observed by Ran et al. (2014) is due to an increase in particle–drop interactions in the accretion disks of the standing wave field, at least at the conditions explored by those authors. In addition to this, a model was developed to explain the increased scavenging data observed by Ran et al. (2014). This model replicated the relationship between the increase in scavenging due to ultrasonics and the air and water flow rates, observed by Ran et al. (2014). Further analysis was presented which suggests that the ultrasonic scrubber should work even more effectively at the higher particle concentrations typical of industrial applications. Specifically, it was suggested that at these higher concentrations, the particle–particle interactions which were shown to be unimportant in the work of Ran et al. (2014) would contribute significantly.

Acknowledgements

This work was funded by NIOSH and NSF (Award #1336632) whose support is gratefully acknowledged. The authors thank Dr. R. Glynn Holt, Steven Fredericks, and Tyler Merrell for helpful discussions on several aspects of the work presented herein.

References

- Allen, E., & Smith, P. (2001). A review of particle agglomeration. *Surfaces*, 85, 87.
- Cohen, A.J. (2000). Outdoor air pollution and lung cancer. *Environmental Health Perspectives*, 108, 743–750.
- Davies, C.N. (1945). Definitive equations for the fluid resistance of spheres. *Proceedings of the Physical Society*, 57, 259–270.
- Davis, D.L., Bell, M.L., & Fletcher, T.A. (2002). A look back at the London smog of 1952 and the half century since. *Environmental Health Perspectives*, 110, A734–A735.
- Docker, D.W., & Pope, C.A. (1994). Acute respiratory effects of particulate air pollution. *Annual Review of Public Health*, 15, 107–132.
- Gemci, T., & Ebert, F. (1992). Prediction of the particle capture efficiency based on the combined mechanisms by a 3-D simulation of a wet scrubber. *Journal of Aerosol Science*, 23, 769–772.
- Greenfield, S.M. (1957). Rain scavenging of radioactive particulate matter from the atmosphere. *Journal of Meteorology*, 14, 115–125.
- Hancock, A. (2001). Observation of forces on microparticles in acoustic standing waves (Master's thesis). Davis: University of California.
- Happel, J., & Brenner, H. (1965). *Low Reynolds Number Hydrodynamics with Special Applications to Particulate Media*. Prentice-Hall: Englewood Cliffs, NJ.
- Hinds, W.C. (1999). *Aerosol Technology: Properties, Behavior, and Measurement of Airborne Particles*. John Wiley & Sons: New York, NY.
- Hinds, W.C. (1982). *Aerosol Technology, Properties, Behavior, and Measurement of Airborne Particles*. Wiley-Interscience: New York, NY.
- Hoffman, K.A., & Chiang, S.T. (2000). *Computational Fluid Dynamics*. Engineering Education System: Wichita, KS.
- Johnson, R.L. (2004). Relative effects of air pollution on lungs and heart. *Circulation*, 109, 5–7.
- Kim, H.T., Jung, C.H., Oh, S.N., & Lee, K.W. (2001). Particle removal efficiency of gravitational wet scrubber considering diffusion, interception, and impaction. *Environmental Engineering Science*, 18, 125–136.
- Lai, K.Y., Dayan, N., & Kerker, M. (1978). Scavenging of aerosol particles by a falling water droplet. *Journal of the Atmospheric Sciences*, 35, 674–682.
- Lee, K., & Chen, H. (1984). Coagulation rate of polydisperse particles. *Aerosol Science and Technology*, 3, 327–334.
- Lim, K.S., Lee, S.H., & Park, H.S. (2006). Prediction for particle removal efficiency of a reverse jet scrubber. *Journal of Aerosol Science*, 37, 1826–1839.
- Otto, E., & Fissan, H. (1999). Brownian coagulation of submicron particles. *Advanced Powder Technology*, 10, 1–20.
- Panton, R.L. (1984). *Incompressible Flow*. John Wiley & Sons: New York, NY.
- Pope, C.A., Burnett, R.T., Thun, M.J., Calle, E.E., Krewski, D., Ito, K., & Thurston, G.D. (2002). Lung cancer, cardiopulmonary mortality, and long-term exposure to fine particulate air pollution. *JAMA*, 287, 1132–1141.
- Pope, C.A., Burnett, R.T., Thurston, G.D., Thun, M.J., Calle, E.E., Krewski, D., & Godleski, J.J. (2004). Cardiovascular mortality and long-term exposure to particulate air pollution. *Circulation*, 109, 71–77.
- Pope, C.A., Thun, M.J., Namboodiri, M.M., Dockery, D.W., Evans, J.S., Speizer, F.E., & Heath, C.W. (1995). Particulate air pollution as a predictor of mortality in a prospective study of U.S. adults. *American Journal of Respiratory and Critical Care Medicine*, 151, 669–674.
- Raj Mohan, B., Jain, R.K., & Meikap, B.C. (2008). Comprehensive analysis for prediction of dust removal efficiency using twin-fluid atomization in a spray scrubber. *Separation and Purification Technology*, 63, 269–277.
- Ran, W., Saylor, J.R., & Holt, R.G. (2014). Improved particle scavenging by a combination of ultrasonics and water sprays. *Journal of Aerosol Science*, 67, 104–118.
- Schikowski, T., Sugiri, D., Ranft, U., Gehring, U., Heinrich, J., Wichmann, H.-E., & Kramer, U. (2005). Long-term air pollution exposure and living close to busy roads are associated with COPD in women. *Respiratory Research*, 6, 152.

- Schwartz, J., & Dockery, D.W. (1992). Increased mortality in Philadelphia associated with daily air pollution concentrations. *American Review of Respiratory Disease*, 145, 600–604.
- Schwartz, J., Laden, F., & Zanobetti, A. (2002). The concentration–response relation between PM_{2.5} and daily deaths. *Environmental Health Perspectives*, 110, 1025–1029.
- Schwartz, J., Slater, D., Larson, T.V., Pierson, W.E., & Koenig, J.Q. (1993). Particulate air pollution and hospital emergency room visits for asthma in Seattle. *American Review of Respiratory Disease*, 147, 826–831.
- Seaton, A., MacNee, W., Donaldson, K., & Godden, D. (1995). Particulate air pollution and acute health effects. *The Lancet*, 345, 176–178.
- Settnes, M., & Bruus, H. (2012). Forces acting on a small particle in an acoustical field in a viscous fluid. *Physical Review E*, 85, 016327.
- Shannon, P., Gorman, L.J., & Reichel, M. (2013). *Particulate Pollutant System Study: Fine Particle Emissions, Vol. II*. U.S. Environmental Protection Agency.
- Slinn, W.G.N. (1984). Precipitation scavenging. *Atmospheric Science and Power Production*, 466–532.
- Suwa, T., Hogg, J.C., Quinlan, K.B., Ohgami, A., Vincent, R., & van Eeden, S.F. (2002). Particulate air pollution induces progression of atherosclerosis. *Journal of the American College of Cardiology*, 39, 935–942.
- Taneda, S. (1956). Experimental investigation of the wake behind a sphere at low Reynolds numbers. *Journal of the Physical Society of Japan*, 11, 1104–1108.
- Tucker, W.G. (2000). An overview of PM_{2.5} sources and control strategies. *Fuel Processing Technology*, 65–66, 379–392.
- Verrier, R.L., Mittleman, M.A., & Stone, P.H. (2002). Air pollution: an insidious and pervasive component of cardiac risk. *Circulation*, 106, 890–892.
- Zamyshlyayev, A., & Shrager, G. (2004). Fluid flows past spheroids at moderate Reynolds numbers. *Fluid Dynamics*, 39, 376–383.